Wind and Structures, *Vol. 11, No. 1 (2021) 1–22*
DOI: http://dx.doi.org/2021.1111

Experimental characterization of the lateral and near-wake flow for the BARC configuration

E. Pasqualetto[1a], G. Lunghi[1b], B. Rocchio[1c], A. Mariotti*[1] and M.V. Salvetti[1d]

[1]*Dipartimento di Ingegneria Civile e Industriale, Università di Pisa, Via G. Caruso 8, 56122 Pisa, Italy*

(Received keep as black, Revised keep as black, Accepted keep as black)

Abstract. We experimentally investigate the high-Reynolds flow around a rectangular cylinder of aspect ratio 5:1. This configuration is the object of the international BARC benchmark. Wind tunnel tests have been carried out for the flow at zero angle of attack and a Reynolds number, based on the crossflow cylinder length and on the freestream velocity, equal, to 40 000. Velocity measurements are obtained by using hot-wire anemometry along 50 different cross-flow traverses on the cylinder side and in the near wake. Differential pressure measurements are acquired on multiple streamwise sections of the model. The obtained measurements are in a good agreement with the state-of-the-art experiments. For the first time among the several contributions to the BARC benchmark, detailed flow measurements are acquired in the region near the cylinder side and in the near-wake flow. The edges and the thickness of the shear layers detaching from the upstream edges are derived from velocity measurements. Furthermore, we compute the flow frequencies characterizing the roll-up of the shear layers, the evolution of vortical structures near the cylinder side and the vortex shedding in the wake.

Keywords: BARC benchmark; wind-tunnel experiments; hot-wire anemometry; pressure measurements; lateral and near-wake flow features

1. Introduction

The present work is aimed at experimentally investigating the high-Reynolds flow around a rectangular cylinder of aspect ratio 5:1, defined as the ratio between the streamwise length, L, over the crossflow one, D. The considered Reynolds number is $Re = DU_\infty/\nu = 40\,000$, being U_∞ the freestream velocity and ν the fluid viscosity, and the angle of attack is equal to zero. This configuration is the object of the international initiative, BARC − Benchmark on the Aerodynamics of a Rectangular 5:1 Cylinder (*http://www.aniv-iawe.org/barc*) and it

*Corresponding author, Alessandro Mariotti, E-mail: alessandro.mariotti@for.unipi.it
[a]E-mail: elena.pasqualetto@phd.unipi.it
[b]E-mail: gianmarco.lunghi@phd.unipi.it
[c]E-mail: benedetto.rocchio@ing.unipi.it
[d]E-mail: maria.vittoria.salvetti@unipi.it

ISSN: (Print), (Online)

can be considered relevant for wind-engineering applications. For instance, tall buildings are often shaped as elongated prisms and two-dimensional rectangular cylinders have commonly been considered as a qualitative schematizations of bridge decks (see, e.g., Matsumoto 1996). Despite the simple geometry, the related flow dynamics is really complex: the shear-layer separated from the upstream edge starts to roll-up forming vortical structures of different size and the corresponding mean flow is characterized by a recirculation region ending by reattachment close to the trailing edge; furthermore, downstream in the wake, the classical vortex shedding occurs.

Experimental and numerical investigations have been carried out by several research groups worldwide, many of them reviewed in the paper by Bruno *et al.* (2014). Among the main experimental results, it is worth reminding the first experiments by Matsumoto *et al.* (2003), those by Bronkhorst *et al.* (2011) and the measurements in a high-pressure wind tunnel performed by Schewe (2013), who investigated a wide range of Reynolds numbers ($Re = 4000 - 600\,000$). More recently, Nguyen *et al.* (2018) carried out low-turbulence experiments (turbulence intensity $I_u \leq 0.2\%$), whereas the effects of free-stream turbulence in the range $I_u = 0.7\% - 13.6\%$ on the bulk quantities and flow features was measured by Mannini *et al.* (2017) in the range $Re = 11\,800 - 112\,600$. Lander *et al.* (2018), Moore *et al.* (2019) and Moore and Amitay (2021) carried out velocity measurements in the detaching shear layers, focusing on the energetic scales and on the production and evolution of the turbulent kinetic energy. Moreover, in Schewe (2013), Mannini *et al.* (2017) and Wu *et al.* (2020) the effects of a non-zero angle of attack of the incoming flow on the bulk quantities, pressure distributions and flow features have been discussed. Besides those reviewed in Bruno *et al.* (2014), more recent data are also available from numerical simulations, including Large Eddy Simulations (Patruno *et al.* 2016, Mariotti *et al.* 2017, Ricci *et al.* 2017, Mannini *et al.* 2019, Rocchio *et al.* 2020, Zhang and Xu 2020, Wu *et al.* 2020) and unsteady RANS (Patruno *et al.* 2016, Mariotti *et al.* 2016). Recently, Direct Numerical Simulations at moderate Reynolds number ($Re = 3000$) have been carried out by Cimarelli *et al.* (2018), Cimarelli *et al.* (2018b) and Chiarini and Quadrio (2021).

The review by Bruno *et al.* (2014) pointed out a significant dispersion in the pressure distribution over the cylinder lateral sides, and, hence, for the oscillating lift as well, both in experiments and numerical simulations. This is in turn related with differences in the mean flow topology over the cylinder side and , in particular, in the size of the mean recirculation region. As for numerical studies, the dispersion is remarkable also for “high-fidelity” approaches, like LES, the results being highly sensitive to grid refinement, SGS modeling and corner treatment (Bruno *et al.* 2012, Mariotti *et al.* 2017 and Rocchio *et al.* 2020). As for experiments, Mannini *et al.* (2017) showed that the pressure distribution on the cylinder lateral side is highly impacted by the incoming turbulence. Most of the experiments in the literature provide the pressure distribution over the later side, together with bulk quantities and aerodynamic loads, but not detailed measurements of the flow in the lateral near-wall region. On the other hand, Moore *et al.* (2019) carried out detailed PIV velocity measurements and a valuable analysis of the dynamics of the shear-layer detaching from the upstream edge, whereas not providing pressure measurements on the cylinder surface.

The present work is aimed at systematically investigating the lateral and near-wake flow in terms of experimental pressure distributions and hot-wire velocity measurements. In this work, velocity measurements are taken for 50 different cross-flow traverses along the cylinder side and in the first 2.5 diameters in the near wake. They are complemented by differential pressure measurements acquired on the central section of the wind-tunnel model and on additional 9 streamwise sections equispaced in the spanwise direction.

2. Experimental set-up

The tests were carried out in the closed-return subsonic wind tunnel of the University of Pisa. The wind tunnel has a circular open test section 1.1 m in diameter and 1.42 m in length, and a free-stream turbulence level $I_u = 0.9\%$. The wind tunnel of the University of Pisa has been widely used and validated for investigations on bluff-body flows in the last decades and additional details on the facility can be found, e.g., in Buresti (1981), Buresti *et al.* (1998), Iungo and Buresti (2009), Mariotti and Buresti (2013) and Mariotti *et al.* (2017b). The aluminum-alloy 5:1 model, sketched in Fig. 1 together with the reference system, has a crossflow length equal to $D = 40$ mm and it is extruded in the spanwise direction for $S = 20D$. Since the expected high sensitivity of the aerodynamic behavior of the rectangular cylinder to sharp edges, particular care was devoted to obtain high quality edges. The manufacturing curvature radius of the upstream edges, evaluated by using the digital microscope RS PRO, is equal to $r/D = 5 \times 10^{-4}$.

Two end plates are placed at the lateral sides of the model, i.e. at $z/D = \pm 10$, in order to reduce three-dimensional effects. The end plates have a semi-circular front part with diameter equal to $d = 10D$, a rectangular rear part $20D \times 10D$ and thickness equal to $0.25D$. End plates extend $8D$ upstream, $12D$ downstream and $4.5D$ in both cross-stream directions and have a rounded leading edge to avoid boundary-layer separation (see e.g. Byrne *et al.* 2019). Two faired struts support the model and the end plates allowing also

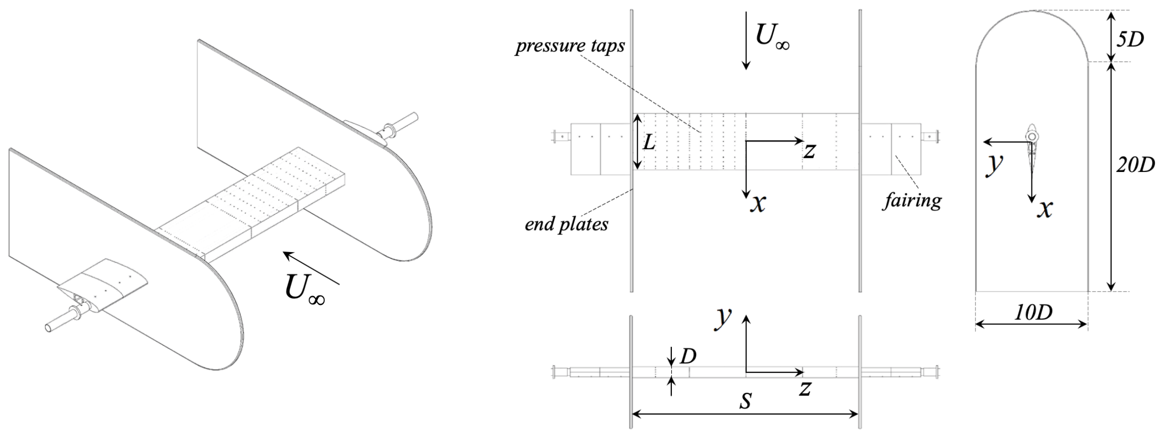

Fig. 1 Sketch of the experimental set-up and reference system: isometric view (a) and plane view (b)

Fig. 2 Experimental model and pressure taps

to accurately set the angle of attack of the model, which is kept fixed to zero degrees in the present investigation. Experiments have been carried out at Reynolds numbers $Re = 40\,000$.

The model has 396 pressure taps over the lateral surfaces, 27 taps over the front face and 72 taps over the rear face, distributed along 12 streamwise sections (see Fig. 1 and Fig 2). In particular, streamwise sections at $z/D = 0$ and $z/D = \pm 5$ have 54 taps on the lateral surfaces (27 on the top surface and 27 on the bottom one), 9 taps over the front face and 9 over the rear face each. Additional 8 streamwise sections, equally spaced at $z/D = 1$ between $z/D = 0$ and $z/D = 9$, and the streamwise section at $z/D = -8$ have 26 taps on the lateral surfaces (13 top and 13 bottom) and 5 taps on the rear face. The model can be also turned upside down to obtain the pressure spanwise distribution over the bottom lateral face. The positions of pressure taps are summarized in Table 1. The local abscissa, s/D, is the distance from the cylinder stagnation point, which is located at $(x/D, y/D) = (-2.5, 0)$, measured along the cylinder side. The pressures were measured using two Pressure Systems ESP-16HD miniature electronic pressure scanners, directly positioned inside the model with the relevant output cables passing through the support fairing.

The velocity measurements to obtain the lateral and the wake field were carried out by using an IFA AN 1003 A.A. Lab System hot-wire anemometry module. X-wire Dantec 55P61 probes could be moved in the x, y and z directions with an accuracy of 0.1 mm by means of a computer-controlled traversing system. Two sets of preliminary tests have been

Table 1 Summary of the positions of pressure taps

Streamwise section	s/D
z/D=0, z/D= ±5	0 0.1 0.2 0.3 0.4 0.6 0.7 0.8 0.9 1.05 1.2 1.4 1.6 1.8 2.2 2.4 2.6 2.8 3.0 3.2 3.4 3.6 3.8 4.2 4.4 4.6 4.8 4.95 5.1 5.2 5.3 5.4 5.6 5.7 5.8 5.9 6.0
z/D=1, z/D=2, z/D=3, z/D=4, z/D=6, z/D=7, z/D=±8, z/D=9	0.6 0.8 1.2 1.6 2.2 2.6 3.0 3.4 3.8 4.4 4.8 5.2 5.4 5.6 5.8. 6.0

performed to choose the measurement period and the sampling frequency of signals, both for differential pressure and velocity measurements. As for the measurement period, we checked that the mean values and the statistical moments up to the third order for pressure and velocity signals did not change comparing a signal acquired for 32.768 s (2^{19} samples at 16 000 Hz) and one acquired for 65.536 s (2^{20}samples at 16 000 Hz). Since no differences were found, 32.768 s was chosen as measurement period. Regarding the sampling frequency, we compared the spectral power density of the Fourier spectra of pressure and velocity signals acquired at 16 000 Hz and 32 000 Hz. No significant spectral content was present above 8000 Hz and, thus, 16 000 Hz was chosen as sampling frequency. These acquisition parameters allowed us to obtain an adequate frequency resolution for characterizing Kelvin-Helmholtz instability in the detaching shear layers and stationary values of the central moments up to the third order for all the fluctuating quantities.

3. Results and discussion

In this section the experimental results are presented and compared with the previous contributions to the BARC benchmark. First we consider the pressure coefficient C_p, which is defined as follows (e.g., Mariotti *et al.* 2014, 2015 and Mariotti *et al.* 2017b):

$$C_p = \frac{p - p_\infty}{1/2 \rho U_\infty^2} \tag{1}$$

where p is the local pressure, ρ is the density and p_∞ is the freestream pressure. The distribution of the experimental pressure coefficient averaged in time and between the upper and lower half perimeters of the cylinder and denoted with $\langle C_p \rangle$ is shown for the streamwise section $z/D = 0$ in Fig. 3a. According to Dekking (2005), error bars correspond to the random measurement error evaluated as $\pm 2\sigma(\langle C_p \rangle)/\sqrt{N-1}$, with $\sigma(\langle C_p \rangle)$ being the standard deviation of N different evaluations of the $\langle C_p \rangle$ from N signals acquired at different time instants. The time standard deviation of the pressure coefficient, $\sigma(C_p)$ and the relevant error bars, derived from the pressure signals by means of an analogous procedure, are reported in Fig. 3b. The distributions of $\langle C_p \rangle$ and of $\sigma(C_p)$ are compared with the ensemble statistics of the BARC experiments (from Bruno *et al.* 2014), given in terms of median, 25th and 75th percentile values, p_{25} and p_{75}, (boxes), whiskers (bars) and outliers (crosses), if any. In these statistics, points are drawn as outliers if the relative values are larger than $p_{75} + \beta(p_{75} - p_{25})$ or smaller than $p_{25} - \beta(p_{75} - p_{25})$, $\beta = 1.5$ being the maximum whisker length.

In the review of Bruno *et al.* (2014) a significant dispersion of the distributions of $\langle C_p \rangle$ and of $\sigma(C_p)$ is observed. The present mean pressure distribution is very close to the 50th percentile of the ensemble statistics of the BARC results (red lines) and all the experimental data falls between the 25th and the 75th percentiles. As for pressure fluctuations, the agreement with the BARC statistics is again very good for $s/D \leq 4$, whereas experimental values above the 75th percentile of BARC statistics are found for $s/D > 4$. In the present experimental data the maximum value of $\sigma(C_p)$ is located at $s/D = 4.4$, slightly downstream of the one found in most of the experimental contributions reviewed in Bruno *et al.* (2014). It should be noted that such point is found to be strictly related to the length of the mean recirculation region on the lateral side of the model (Rocchio *et al.* 2020, Lunghi *et al.* 2021) and, thus, it is reasonable to infer that this recirculation is slightly longer in the present experiments than in most of the experimental contributions reviewed in Bruno *et al.* (2014). The longer mean recirculation length implies, in turn, that the maximum pressure fluctuation occurs more downstream than in most of the BARC experiments. In our opinion, the main reason of the differences with some of the experimental contributions to BARC is the inlet turbulence. The effect of the inlet turbulence has been discussed in Mannini *et al.* (2017), in which it was observed that the higher the inlet turbulence is the lower the length of the mean recirculation region is. In our experiments we have low turbulence intensity (0.9%) of the oncoming flow. This is consistent with the slightly longer recirculation region we obtain compared with the ensemble statistics of the BARC experiments, which were mostly carried out for higher values of the turbulence intensity. The similarity of the present results to the experiments by Mannini *et al.* (2017), carried out with a turbulence intensity of 0.7%, supports this explanation. However, we cannot exclude *a priori* that other set-up parameters (rounding of the upstream edges, turbulence scale, ...) may have some effect on the results and on the length of the recirculation region.

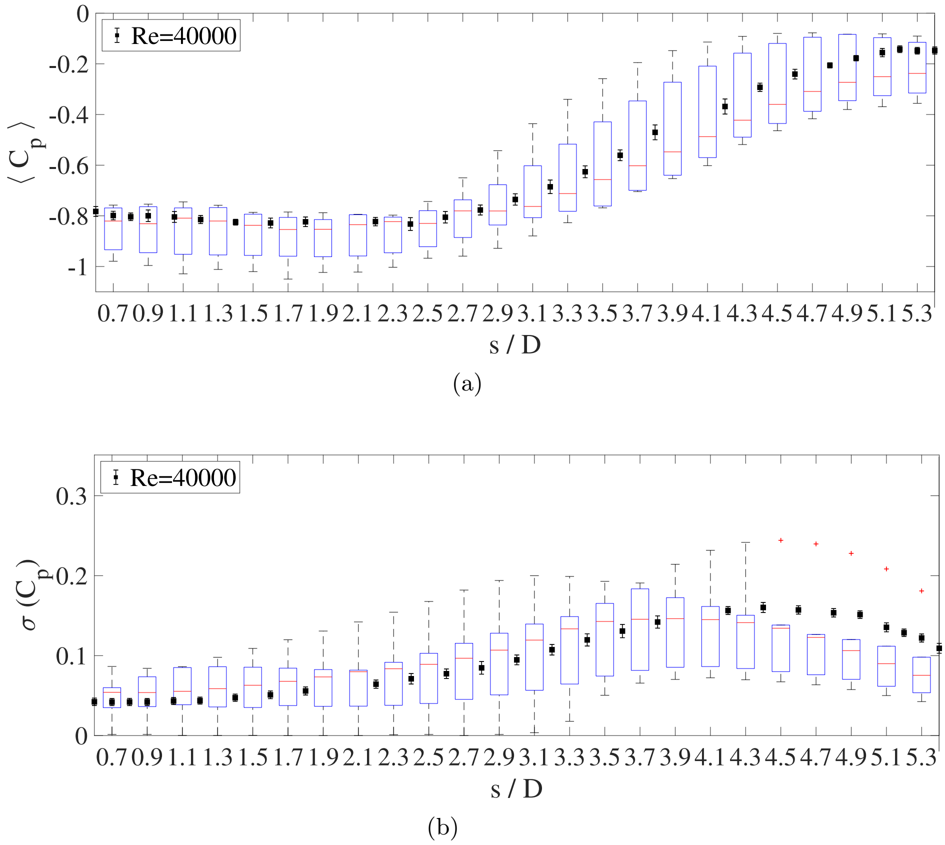

Fig. 3 Experimental mean pressure coefficient $\langle C_p \rangle$ (a) and its standard deviation $\sigma(C_p)$ (b) (black squares). Comparison with the ensemble statistics of the BARC experiments (boxes, bars and crosses) revised in Bruno *et al.* (2014)

The distributions of $\langle C_p \rangle$ and $\sigma(C_p)$ are compared with the recent experiments by Schewe (2013), Mannini *et al.* (2017), Nguyen *et al.* (2018), Wu *et al.* (2020) in Fig. 4a and Fig. 4b, respectively. These experiments are carried out for Reynolds numbers in the range 41 600 − 56 700 and are not included in the statistics shown in Fig. 4. Despite the experimental and numerical results are obtained at slightly different Reynolds numbers, all the considered results fall inside the low-sensitivity region with Reynolds. Indeed, low Reynolds-number effects are found for $10\,000 \leq Re \leq 200\,000$, whereas significant Reynolds-number effects are expected for $Re \leq 10\,000$ and $Re \geq 200\,000$ (see Schewe 2013 and Mannini *et al.* 2010). All the $\langle C_p \rangle$ data closely agree, whereas $\sigma(C_p)$ is characterized by a higher dispersion. Excellent agreement is found with the distribution obtained in the experiments by Mannini *et al.* (2017). The position of maximum $\sigma(C_p)$ is also close to that measured in Wu *et al.* (2020), even though the latter experiments give a significant larger value of this maximum. The averaged differences between the results obtained in the present experiment and the literature data set are quantitatively evaluated by using the L_2 norm of the differences and indicated with Δ_{L_2}. Moreover, the maximum differences in pressure and velocity values are evaluated

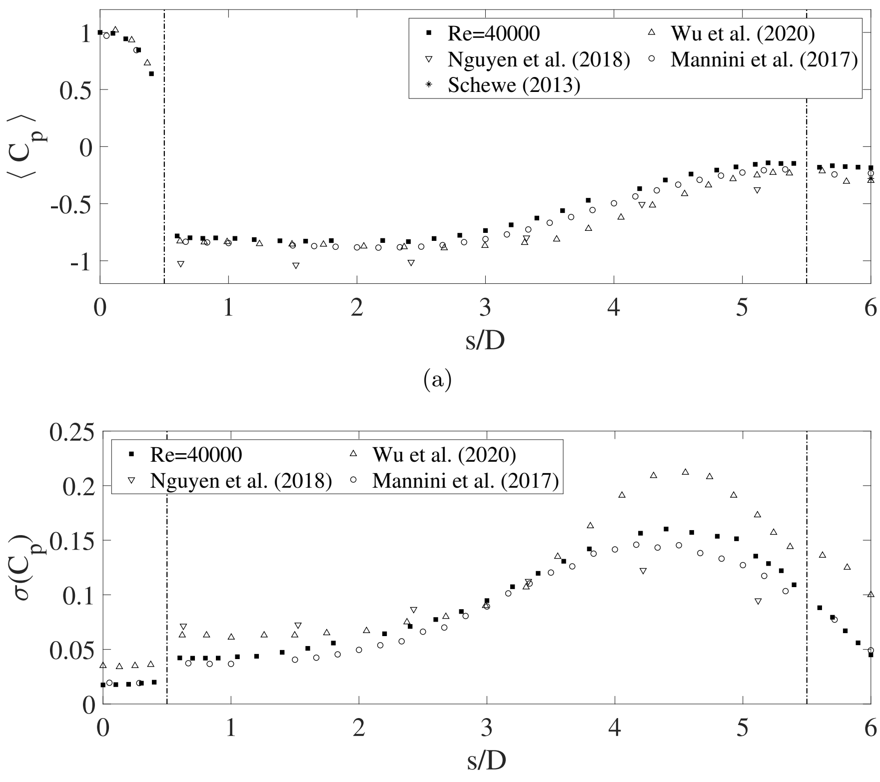

Fig. 4 Experimental mean pressure coefficient $\langle C_p \rangle$ (a) and its standard deviation $\sigma(C_p)$ (b). Comparison with experimental results from Nguyen *et al.* (2018) at $Re = 41\,600$, Wu *et al.* (2020) at $Re = 53\,600$, Schewe (2013) at $Re = 54\,200$ and Mannini *et al.* (2017) at $Re = 56\,700$.

by using the L_∞ norm and indicated with Δ_{L_∞}. As for Fig. 4a, the averaged differences of the mean pressure distribution with the result in Mannini *et al.* (2017) is very low and equal to $\Delta_{L_2}(\langle C_p \rangle) = 0.0683$; while the ones with the results in Nguyen *et al.* (2018) and Wu *et al.* (2020) are slightly larger, viz. $\Delta_{L_2}(\langle C_p \rangle) = 0.1911$ and $\Delta_{L_2}(\langle C_p \rangle) = 0.1276$, respectively. Maximum discrepancies are again lower with Mannini *et al.* (2017), i.e. $\Delta_{L_\infty}(\langle C_p \rangle) = 0.186$, rather than with Wu *et al.* (2020) and Nguyen *et al.* (2018), which are equal to $\Delta_{L_\infty}(\langle C_p \rangle) \approx 0.3$. As for the distributions of the pressure fluctuations reported in Fig. 4b, a very low difference is again found with the results in Mannini *et al.* (2017), i.e., $\Delta_{L_2}(\sigma(C_p)) = 0.0096$, whereas $\Delta_{L_2}(\sigma(C_p)) = 0.03$ is found with Nguyen *et al.* (2018) and Wu *et al.* (2020).

Figures 5(a,c) show the spanwise distributions of the experimental mean pressure coefficient and of its standard deviation, respectively. Sectional plots are also reported in Figs. 5(b,d). Analogous results are obtained for the bottom part of the model, which are not shown here for the sake of brevity. It is clear from Figs. 5(a,b) that the mean pressure coefficient distribution does not significantly change in the spanwise direction in the whole range $0 \leq z/D \leq 9$, whereas negligible differences are observed for $\sigma(C_p)$ in the range $0 \leq z/D \leq 6$ (see Figs. 5(c,d)). Thus, border effects are not found in the range $0 \leq z/D \leq 6$. This allows sensible comparisons with numerical simulations assuming an infinite spanwise length. In addition to this, the correlation of the pressure coefficient in the spanwise direction is shown in Figs. 5(e,f), together with the correlation length, L_{corr} (square symbols and grey line). According to Mariotti *et al.* (2019), the correlation length is computed as follows:

$$L_{corr} = \int_{z/D=0}^{z/D=9} \rho_p(z)dz = \int_{z/D=0}^{z/D=9} \frac{\overline{p(0)p(z)}}{\sigma_p^2} dz \tag{2}$$

where $\rho_p(z)$ is the correlation between the pressure signals $p(0)$ and $p(z)$ contemporaneously acquired at $z/D = 0$ and z/D and σ_p^2 is their variance. The integration is made until $z/D = 9$, where the last streamwise section of pressure taps is located. However, as can be seen from Fig. 5f, where the values of $\rho_p(z)$ in the spanwise direction are reported, the contribution of the part that can be influenced by the presence of the end plates is negligible. A longer correlation length of the pressure coefficient in the spanwise direction is found in the regions near the upstream edge ($0.5 \leq s/D \leq 1.5$) and near the mean reattachment location ($3.5 \leq s/D \leq 4.5$), while in the mean recirculation zone ($1.5 \leq s/D \leq 3.5$) and in the last diameter upstream of the base it assumes lower values. Higher pressure correlations at the upstream edges and in the pressure recovery region are in a good agreement with the numerical results in Bruno *et al.* (2012). The averaged value of the correlation length is equal to $2.1D$, and its maximum value, i.e. $2.7D$, is reached only at the upstream edge. This confirms that a suitable computational domain in numerical simulations should be extruded at least for two times the averaged correlation length, i.e. $4.2D$, in the spanwise direction, together with the imposition of periodic boundary conditions.

To characterize the near-wake flow features, hot-wire measurements along cross-flow traverses were taken at different positions on the lateral side and downstream of the model. We apply the same analysis procedure described in Mariotti and Buresti (2013), Mariotti *et al.* (2017b) and Mariotti (2018). For the sake of completeness, the procedure is briefly recalled herein. We refer, as an example, to Fig. 6, which shows the results along the traverses on

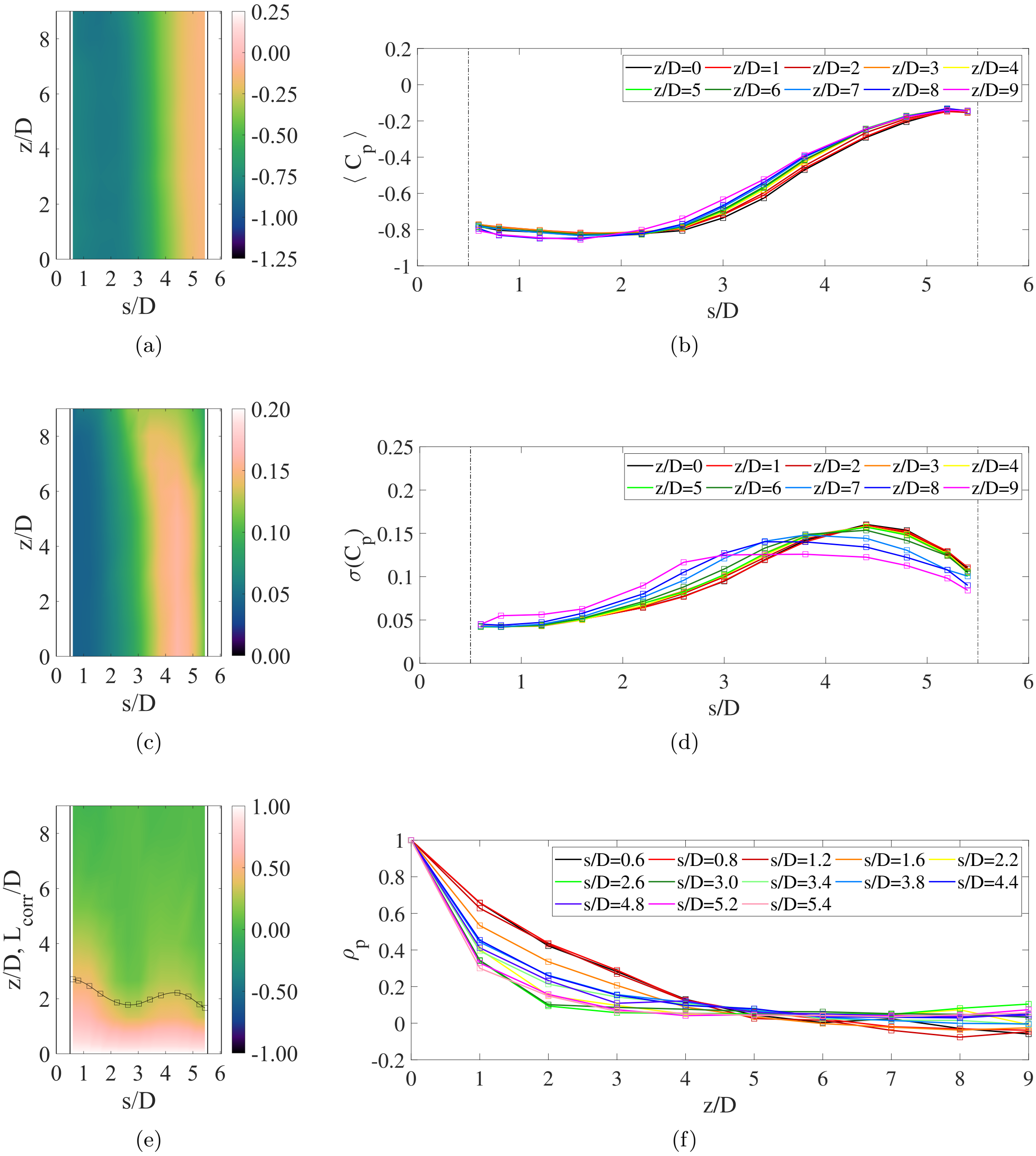

Fig. 5 Spanwise distibution of the mean pressure coefficient $\langle C_p \rangle$ (a), sectional plots of $\langle C_p \rangle$ (b), spanwise distribution of the standard deviation of the pressure coefficient $\sigma(C_p)$ (c), sectional plots of $\sigma(C_p)$ (d), distribution of the correlation of the pressure coefficient in the spanwise direction and correlation length L_{corr} (e), and linear plots on the correlation coefficient in the spanwise direction (f). The results are reported only for the upper face of the cylinder. The end plate is located at $z/D = 10$.

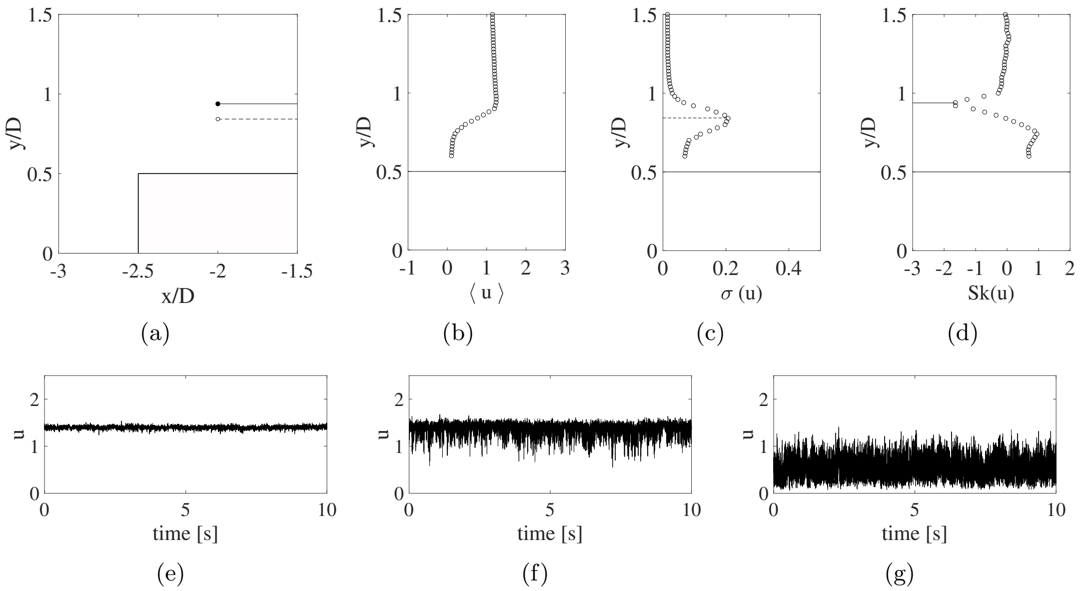

Fig. 6 Construction of the curves of the external edge of the shear layer (black circle (●)) and of the envelope of maximum mean standard deviation (white circle (○)) (a). Profiles of mean streamwise velocity $\langle u \rangle$ (b), of the relative standard deviation $\sigma(u)$ (c) and of the skewness $Sk(u)$ (d) at $x/D = -2.0$. Velocity signals at $x/D = -2.0$ and $y/D = 1.0$ (e), $y/D = 0.9$ (f) and $y/D = 0.8$ (g)

the lateral side of the rectangular cylinder at $x/D = -2$. The mean streamwise velocity $\langle u \rangle$, the standard deviation $\sigma(u)$, and the skewness $Sk(u)$ profiles are shown in Figs. 6b, 6c and 6d, respectively. They are obtained by post-processing hot-wire measured velocity signals at different locations, as, for instance, those shown in Figs. 6e, 6f and 6g for $y/D = 1.0$, $y/D = 0.9$, and $y/D = 0.8$, respectively. The peaks of the standard deviation profile represent the positions of the maximum fluctuations, whereas the negative peaks of the skewness are used here, as in Mariotti and Buresti (2013), Mariotti *et al.* (2017b) and Mariotti (2018), to identify the external edge of the shear layer detaching from the upstream edge and of the wake. Indeed, when measurements are taken by progressively approaching the external edge of a turbulent shear layer or wake from outside, due to turbulent fluctuations, fluid originating from that edge region occasionally reaches the measurement point, carrying with them their lower mean velocity. Therefore, sporadic bursts of low velocity appear in the output signal of the velocity probe (compare Fig. 6f with Fig. 6e). This hardly affects the mean value and the standard deviation of the velocity signal, but causes its skewness to become more and more negative, reaching a minimum at the shear-layer border.

Figure 7a and Figure 7c show some of the measured profiles of the mean-velocity components in streamwise and crosswise directions in the foremost lateral region, i.e. where the shear layer separates from the upstream edges of the rectangular cylinder. The relative standard deviations are reported in Fig. 7b and Fig. 7d. These measurements are taken for 50 different cross-flow traverses on the lateral flow and in the near wake, i.e. between $x/D = -2.5$ and $x/D = 5$. For each cross-flow traverse, the spacing in the y direction

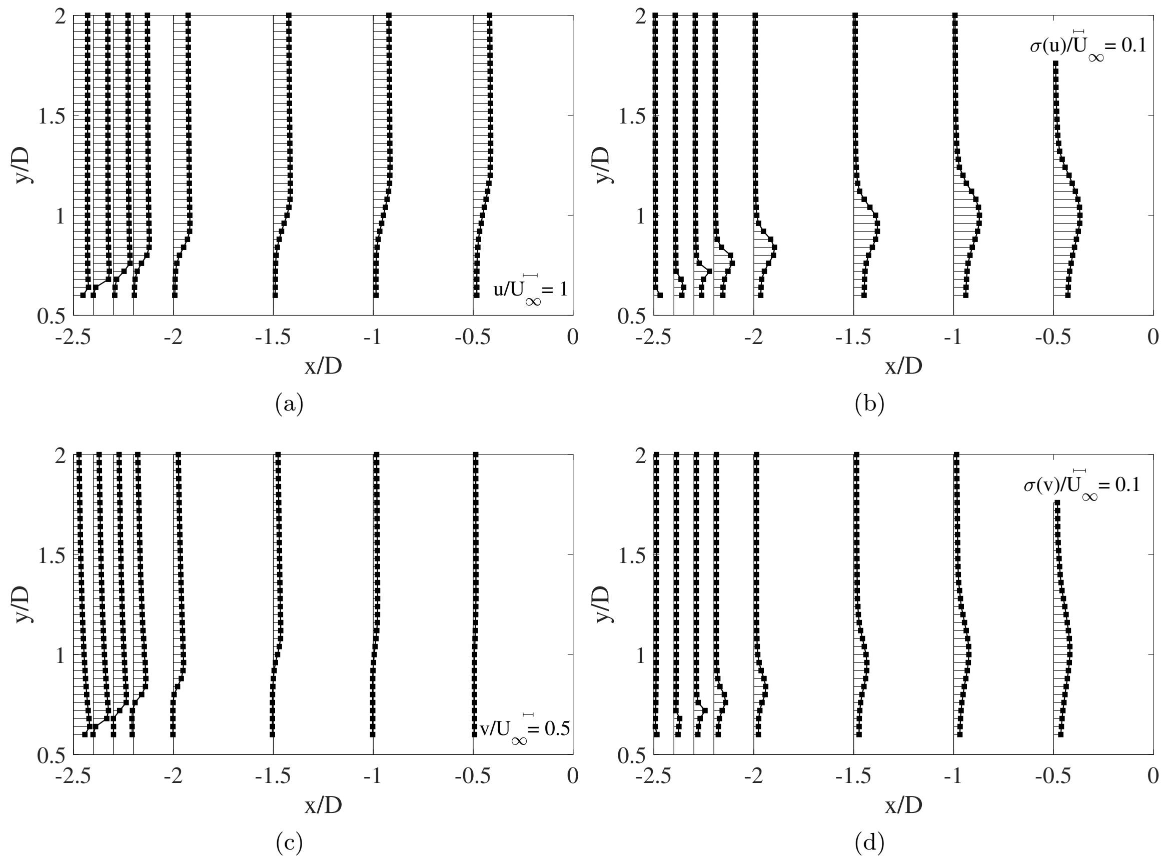

Fig. 7 Profiles of the mean streamwise velocity $\langle u \rangle$ (a), of the standard deviation of the streamwise velocity $\sigma(u)$ (b), of the mean crosswise velocity $\langle v \rangle$ (c), and of the standard deviation of the crosswise velocity $\sigma(v)$ (d).

is $0.025D$. The overall results are presented in Fig. 8. The edge of the shear layer and wake, identified as explained before, are also shown together with the envelope of the maxima of the standard deviation. Note that in these four figures, the obtained values are reported also for the recirculating regions on the lateral side (approximately $0 \leq x/D \leq 2.5$ and $0.5 \leq y/D \leq 1$) and downstream of the body (approximately $2.5 \leq x/D \leq 4$ and $0 \leq y/D \leq 0.5$), where rectification of the hot-wire signals is probably present. Indeed, it is well known that hot-wire/film anemometers rectify the signal outputs due to the lack of sensitivity to flow direction (see, e.g., Yang *et al.* 2010) and they are unable to discern flow direction in a plane normal to the sensing filament. Nevertheless, the shear-layer and wake edges are always outside these recirculation region and thus not affected by rectification issues. Figure 8 gives a glance of the amount and of the detail of the experimental database obtained in the present work, which can be used for investigation and validation.

The experimental results can, for instance, be compared with the available velocity measurements in the detaching shear layers and in the near wake. As for the shear layer, mean

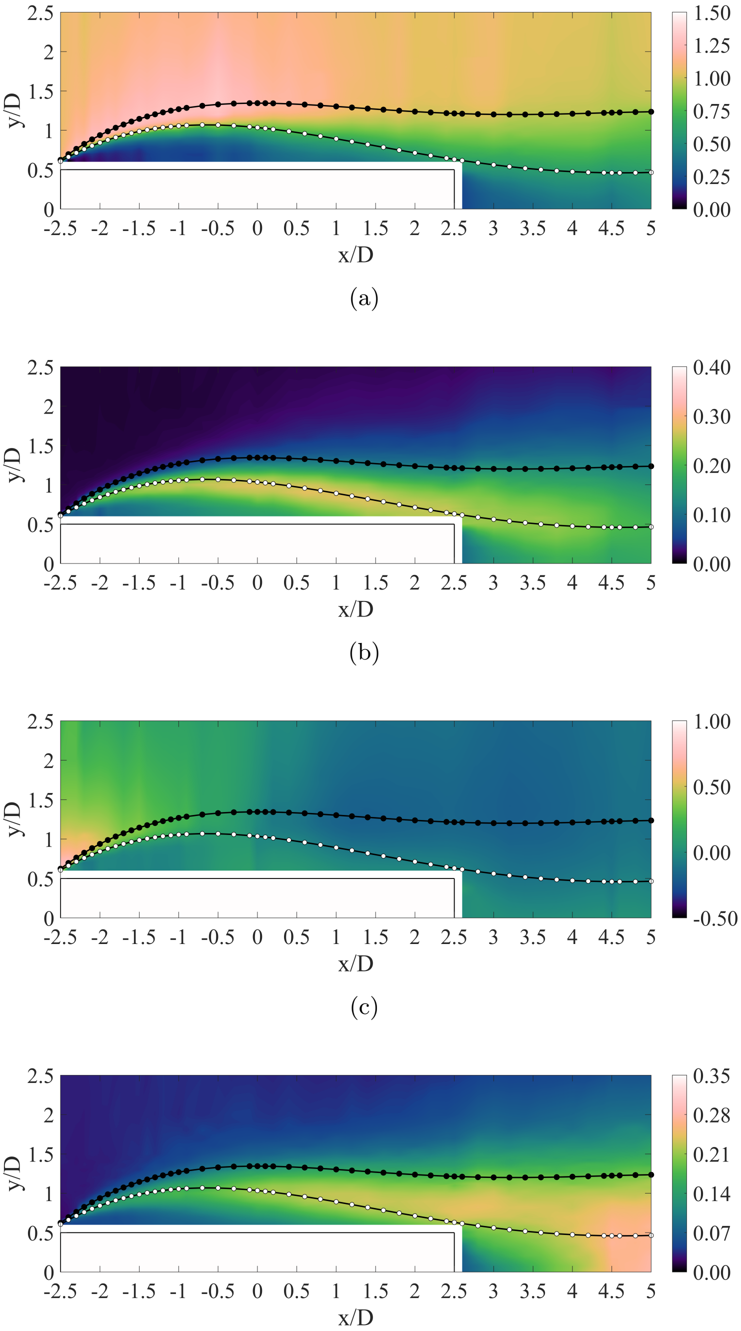

Fig. 8 Mean streamwise velocity field $\langle u \rangle$ (a) and its standard deviation $\sigma(u)$ (b), mean crosswise velocity field $\langle v \rangle$ (c) and its standard deviation $\sigma(v)$ (d). Black circle line (•) indicates the external edge of the shear layer and the wake edge at $Sk(u)$ peaks while white circle line (∘) indicates the envelope of maximum $\sigma(u)$

streamwise velocity and its standard deviation profiles at section $x/D = -2.0$ are shown in Fig. 9(a,b), together with the only available experimental data, which is the one from Mannini *et al.* (2017) at $Re = 11\,800$. Despite the difference in the Reynolds number, the results are in good agreement both for mean velocity and fluctuations. Experimental results are also in good agreement with the mean velocity profile in the LES simulations in Mariotti *et al.* (2017), obtained for 16 different set-ups of the numerical simulations (see Fig. 9c). In particular, the parameters chosen for the sensitivity analysis in Mariotti *et al.* (2017) are the grid resolution in the spanwise direction, defined in terms of the average element size, Δz (in the range $[0.321D, 0.674D]$), and the weight of the explicit filter, w (in the range $[0.01, 0.131]$) that determines the amount of subgridscale dissipation. Experimental data fall inside the uncertainty band also for the standard deviation in time of the streamwise velocity, which is very large (see Fig. 9d). Indeed, it was shown in Mariotti *et al.* (2017) that the flow features in the region close to the lateral side of the cylinder are remarkably sensitive to the above mentioned computational parameters, and a large dispersion of the results was observed.

Focusing now on the near wake, the mean streamwise velocity and fluctuations profile are also compared at the cross section $x/D = 4.5$ with the available experimental and numerical results in Fig. 10(a,b) and Fig. 10(c,d), respectively. Slightly higher values of the mean velocity and of the fluctuations are found compared with the experimental results of Mannini *et al.* (2017). Averaged differences for the x-velocity distributions at $x/D = 4.5$ between the present experiment and the results in Mannini *et al.* (2017) at $Re = 44\,900$ are equal to $\Delta_{L_2}(\langle u \rangle) = 0.0396$ and $\Delta_{L_2}(\sigma(u)) = 0.0128$, respectively. It is reasonable to infer that higher fluctuations in the outer part of the cross-section are possibly related to a higher level of free-stream fluctuations. Indeed, in the present case the free-stream turbulent intensity is equal to 0.9%, whereas it is 0.7% in Mannini *et al.* (2017).

A good agreement is found also with the available numerical results at $x/D = 4.5$. Slightly higher values of $\langle u \rangle$ are also found for $0 \leq y/D \leq 1$ in comparison with the numerical results of Zhang and Xu (2020) at $Re = 40\,000$ and Wu *et al.* (2020) at $Re = 67\,000$, whereas experiments matches the results of the 16 simulations in Mariotti *et al.* (2017). The highest differences in the mean values of the velocity are found between the present experiments and the DNS in Cimarelli *et al.* (2018), carried out at a moderate Reynolds number ($Re = 3000$). A satisfactory agreement in the velocity fluctuations $\sigma(u)$ is found with Wu *et al.* (2020) and Mariotti *et al.* (2017) as can be seen in Fig. 10d. It should be noted that in the simulations in Mariotti *et al.* (2017), in spite of the large differences observed in the flow on the cylinder lateral surface, the dispersion of the results in the wake is small and they are in good agreement with hot-wire velocity fluctuations.

To further investigate the evolution of the shear layers, Fig. 11a shows the vertical position of the characteristic edges of the shear layer, $y_{0.9}(x)$ and $y_{0.1}(x)$, evaluated according to the definition in Pope (2000). For $0 < \alpha < 1$, the location $y_\alpha(x)$ is defined such that $u(x, y_\alpha) = u_i + \alpha(u_e - u_i)$, u_e and u_i being the velocity of the external and the internal stream in the shear layer, respectively. These two shear-layer edges are also compared to the locations of the negative peak of the skewness, used herein to define the external edge of the shear layer and reported with black markers in the same in Fig. 11a. The characteristic width of the shear layer, computed as $\delta_{\mathrm{SL}}(x) = y_{0.9}(x) - y_{0.1}(x)$ (Pope 2000), is then presented

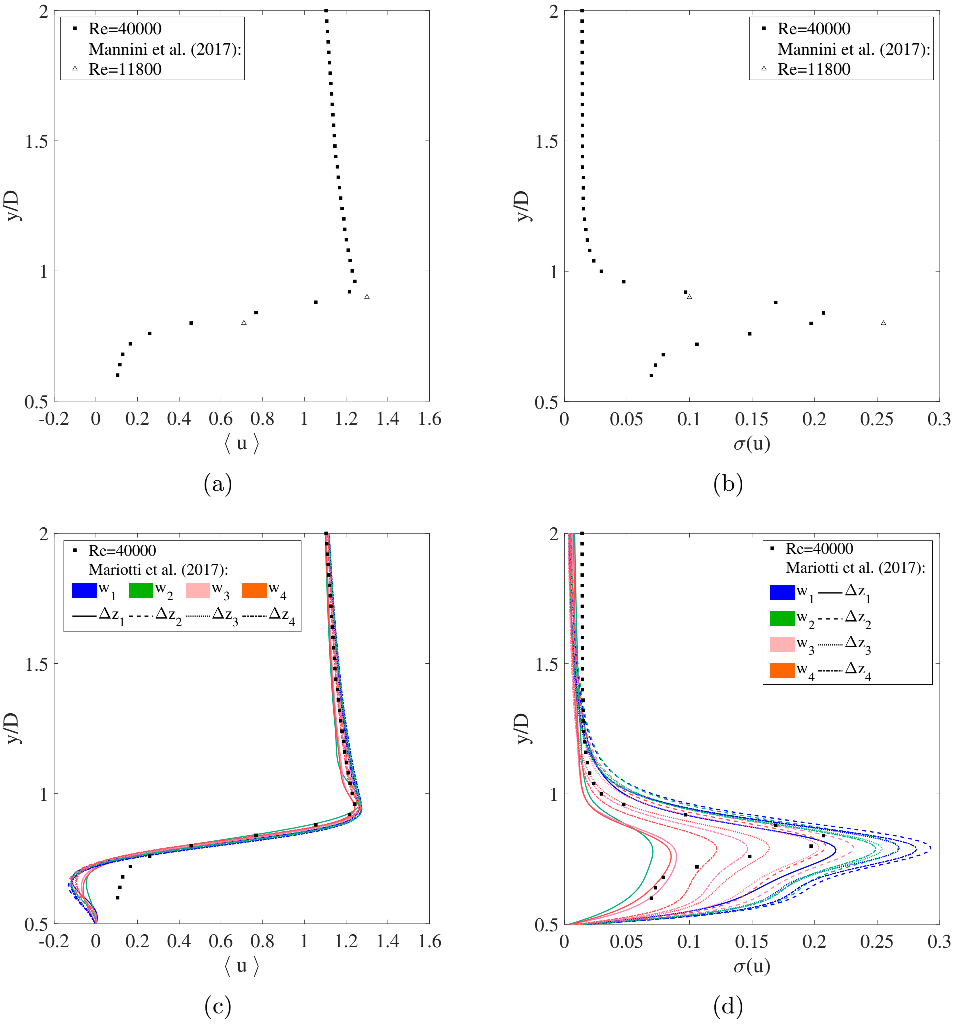

Fig. 9 Profiles of the mean streamwise velocity $\langle u \rangle$ (a,c) and of its standard deviation $\sigma(u)$ (b,d) at section $x/D = -2.0$. Comparison with experimental results from Mannini *et al.* (2017) at $Re = 11\,800$ (a,b) and with the numerical results from Mariotti *et al.* (2017) at $Re = 40\,000$ (c,d).

in Fig. 11b. An almost linear increase of the shear-layer width is found up to $x/D \approx 1$, where a sudden increase of δ_{SL} is present. This occurs where the fluctuation $\sigma^2(u) + \sigma^2(v)$, evaluated on the edge of the shear layer, takes its maximum value. The term $\sigma^2(u) + \sigma^2(v)$ represent the major contribution to the kinetic energy associated to velocity fluctuations (the contribution of $\sigma^2(w)$ is definitely lower as can be seen in Rocchio *et al.* (2020)). In similar works (see e.g. Rocchio *et al.* 2020, Moore *et al.* 2019, Lamballais *et al.* 2010), the kinetic energy associated to velocity fluctuations is also called TKE (Turbulent Kinetic Energy), despite this is not fully appropriate for the considered flow region, in which turbulence is not yet fully developed. The growth of the kinetic energy associated to velocity fluctuations

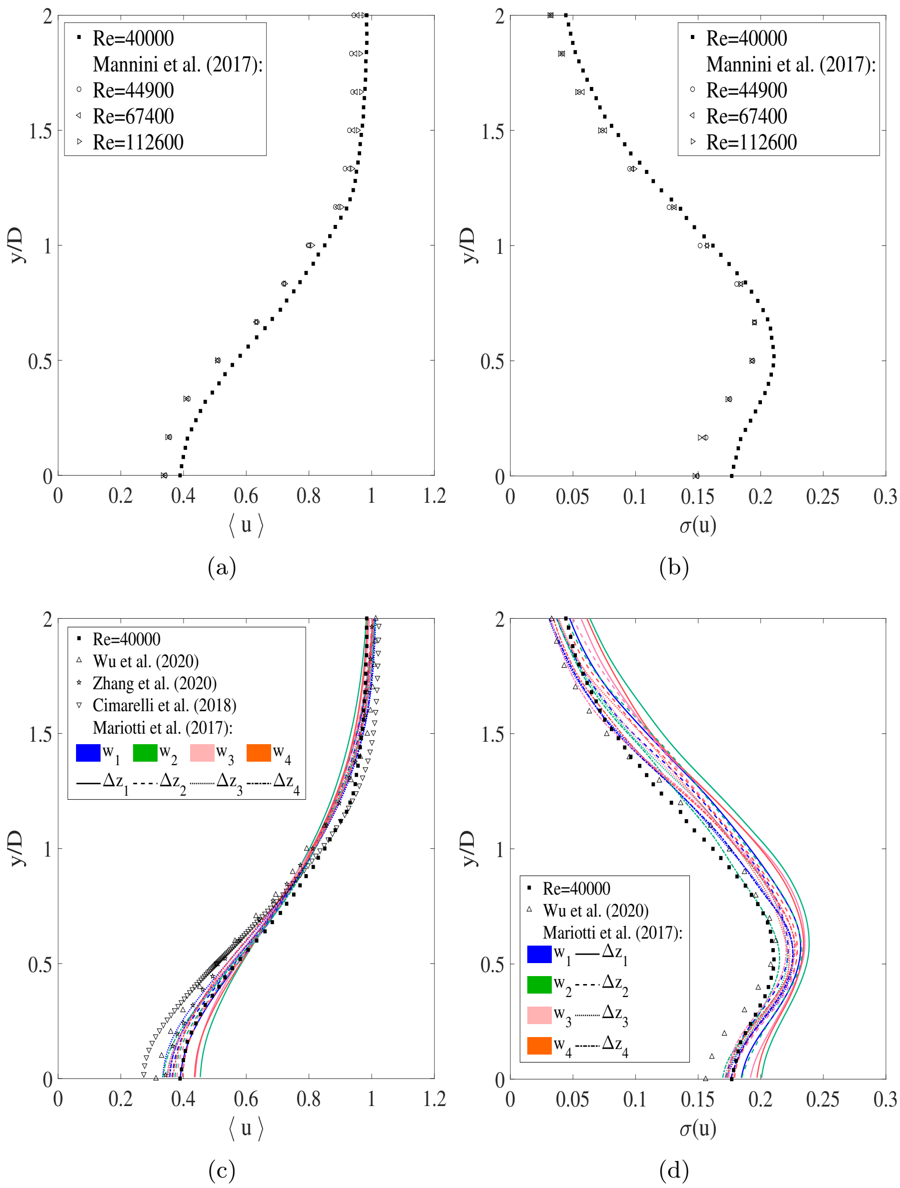

Fig. 10 Profiles of the mean streamwise velocity $\langle u \rangle$ (a,c) and of its standard deviation $\sigma(u)$ (b,d) at section $x/D = 4.5$. Comparison with experimental results from Mannini *et al.* (2017) at different Reynolds numbers (a,b) and with the numerical results from Cimarelli *et al.* (2018) at $Re = 3000$, Zhang and Xu (2020), Mariotti *et al.* (2017) at $Re = 40\,000$ and Wu *et al.* (2020) at $Re = 67\,000$ (c,d).

along the shear-layer external edge is related to the dynamics of the shear layer (roll-up) and, consequently, to the length of the mean recirculation region, as shown in Rocchio *et al.* (2020).

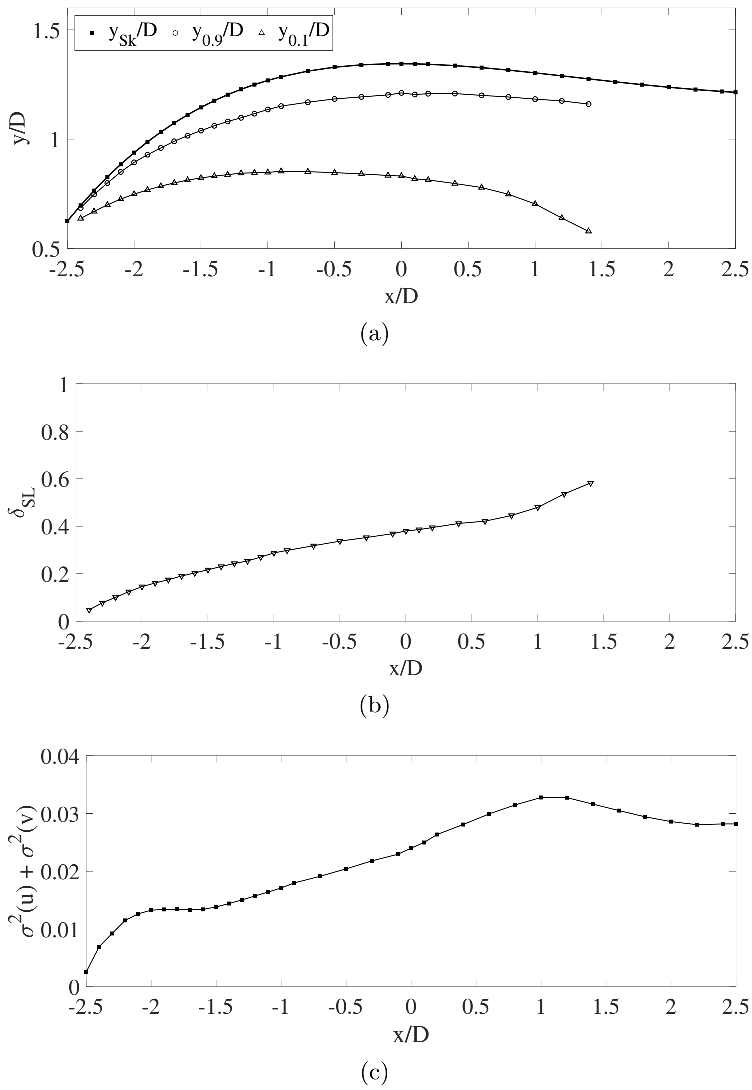

Fig. 11 Characteristic edges of the shear layer, $y_{0.9}(x)$ and $y_{0.1}(x)$, and locations of negative peaks of the skewness (a), characteristic width of the shear layer δ_{SL} (b), values of $\sigma^2(u)+\sigma^2(v)$ evaluated on points of negative peaks of the skewness (c).

The frequency analysis of the hot-wire velocity signals confirms that the increase of the kinetic energy associated to velocity fluctuations along the separated shear layers is related with the Kelvin-Helmholtz instability and, further downstream, to the shear-layer roll-up. Frequency analysis is carried out herein by computing the Welch spectra and the wavelet spectra for some locations slightly outside the shear-layer external edges at different longitudinal positions summarized in Table 2. Figures 12(b,c) present the development of spectral components along the shear layers at the positions indicated in Fig. 12a. The Welch spectra of the $x-$velocity signals are shown, each of them obtained by averaging 10 Fourier

Table 2 Summary of probe location and non-dimensional frequency related to Kelvin-Helmholtz instability, vortex pairing and vortex shedding.

Probe number	Position $(x/D, y/D)$	St_{KH}	St_{VK}
(1)	(-2.50, 0.650)	10.47 - 5.28	-
(2)	(-2.45, 0.675)	10.43 - 5.21	-
(3)	(-2.40, 0.725)	5.11 - 2.68	-
	(-2.35, 0.750)	4.94 - 2.63	-
(4)	(-2.30, 0.800)	2.61	0.114
	(-2.20, 0.850)	2.58	0.114
	(-2.10, 0.900)	2.53 - 1.28	0.114
(5)	(-2.00, 0.950)	1.24 - 0.62	0.114
	(-1.75, 1.075)	0.62	0.114
(6)	(-1.50, 1.175)	0.62	0.114
	(-1.25, 1.225)	0.60	0.114
(7)	(-1.00, 1.300)	0.33	0.114
(8)	(-0.50, 1.350)	0.33	0.114
(9)	(0.00, 1.400)	0.32	0.114
(10)	(0.50, 1.500)	0.24	0.114
(11)	(1.00, 1.500)	0.23	0.114
(12)	(1.50, 1.500)	0.23	0.114
(13)	(2.00, 1.500)	0.23	0.114
(14)	(2.50, 1.500)	0.23	0.114
(15)	(3.00, 1.500)	-	0.114
(16)	(3.50, 1.500)	-	0.114
(17)	(4.00, 1.500)	-	0.114
(18)	(4.50, 1.500)	-	0.114

spectra, and the spectral power density amplitudes have been shifted on the ordinate to allow the comparison of the frequency components. In addition to this, wavelet spectra are derived from the wavelet transform of the $x-$velocity signals, by integrating in time the wavelet maps obtained by employing the complex Morlet wavelet $\Psi(t) = e^{i\omega_0 t}e^{t^2/2}$ and using a central frequency $\omega_0 = 6\pi$. This procedure permits us to obtain spectra which are smoother than the Fourier and Welch ones and well defined from the mathematical point of view (see, e.g., Mariotti and Buresti 2013, Mariotti *et al.* 2017b and Mariotti 2018 for further details on the wavelet procedure), giving a more accurate evaluation of the Kelvin-Helmholtz frequency and of the related sub-harmonics that are reported in Table 2. It should be noted that no characteristic frequencies are found above 2Hz for the empty wind tunnel and, thus, we can exclude effects of these wind-tunnel frequencies in the presented spectra. All the frequencies are expressed in non-dimensional form through the Strouhal number $St = fD/U_\infty$.

As can be observed in Fig. 12b, very close to the separation point, i.e. at $(x/D, y/D) = (-2.5, 0.65)$, a clear peak, corresponding to $St_{KH} = 10.47$, is found together with its primary sub-harmonic at $St = 5.28$. The value of St_{KH} is the typical Kelvin-Helmholtz frequency if

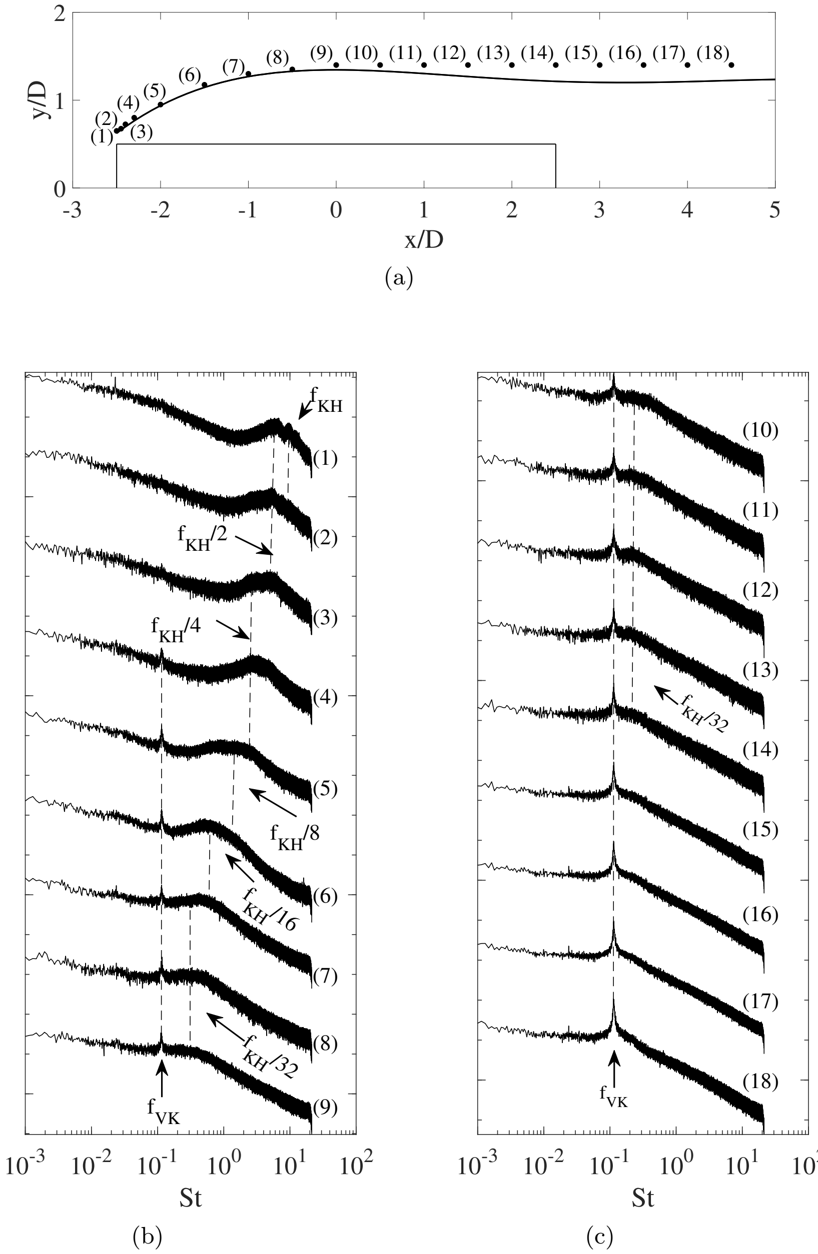

Fig. 12 Probe position (a) and Welch spectra of the $x-$velocity signals (b,c)

rescaled with the local width of the shear layer and it is comparable to the one in Moore *et al.* (2019). Moving further downstream, the Kelvin-Helmholtz frequency disappears and the first sub-harmonic grows in strength until the location $x/D = -2.4$, where it becomes dominant due to the pairing process. At $x/D = -2.3$ the maximum spectral power density is found at $St \approx 2.6$, corresponding to $St_{KH}/4$. In addition to this, the spectral peaks related to both Kelvin-Helmholtz frequency and sub-harmonics shift to lower frequencies moving downstream along the shear layer. This was also experimentally found in Lander *et al.* (2018) for the square section and numerically in Rocchio *et al.* (2020) for the 5:1 section, and it may be associated with a slight reduction in the convection speed of the Kelvin-Helmholtz vortices.

The vortex pairing mechanism is clearly visible up to $St_{KH}/32$, which starts to dominate the Welch and wavelet spectra at $x/D = -0.5$. On the other hand, the vortex shedding frequency at St_{VK} is clearly observed in all the velocity signals acquired downstream of $x/D = -2.3$. A distinctive feature of Figs. 12(b,c) is that between $x/D = 0$ and $x/D = 1$ the spectral peaks at $St_{KH}/32$, approximately equal to 0.33, shift to lower frequency (i.e. $St = 0.23$, which is almost the double the vortex shedding frequency) creating a sort of continuity between these two phenomena. An analogous trend was also highlighted in Moore *et al.* (2019), where a similar migration of energy toward lower frequencies associated with the Von-Karman mode is found.

4. Conclusions

Detailed hot-wire measurements of the lateral and near-wake velocity field are presented together with the pressure distributions on the central section of the wind-tunnel model and on additional 9 streamwise sections equispaced in the spanwise direction. A cross-validation of the pressure and velocity measurements has been provided and a substantial agreement is found with experimental and numerical data in the literature. The detailed velocity measurements permitted to compute the location of the shear layers detaching from the upstream edges and the behavior of the characteristic thickness. The location of the roll-up of the shear-layer has been identified both from the behavior of the fluctuating kinetic energy and from the the frequency analysis of the velocity time signals. This analysis also provided the Kelvin-Helmholtz frequency, related to the shear-layer roll-up, and its sub-harmonics, related to successive vortex pairings. Moreover, a progressive shift to the vortex shedding frequency has been found in the rear part of the body, confirming thus the energy migration scenario also recently observed by Moore *et al.* (2019). Furthermore, the near-wake mean and fluctuating velocity field have also been measured.

Mean pressure coefficient distributions and fluctuations are found in a good agreement with previous studies. The correlation of the pressure coefficient in the spanwise direction, although slightly varying moving along the cylinder later wall, has an average value of 2.1. This confirms that a spanwise length of the computational domain of at least $5D$ should be used in numerical simulations together with periodic boundary conditions.

More generally, the present measurements provide a detailed set of experimental data, enriching the BARC data base and useful for comparison and validation, for instance, of numerical simulations. Moreover, they could also be the reference baseline for future experimental investigations and stochastic sensitivity analysis on the effect of set-up parameters on experimental results, for instance to characterize the effect of the upstream edge roundings or of small variations in the angles of attack.

5. Acknowledgment

The authors wish to thank Guido Buresti for his precious suggestions in the definition of the experimental set-up. Thanks are also due to the technical staff of the Department of Civil and Industrial Engineering (Aerospace Division) for the manufacturing of the wind tunnel model and to Paolo Neri for the measurement of the radius of curvature of the upstream edges.

References

Bronkhorst, A.J., Geurts, C.P.W. and van Bentum, C.A. (2011), "Unsteady pressure measurements on a 5:1 rectangular cylinder", *in: Proceedings of the Thirteenth International Conference on Wind Engineering*, Amsterdam, The Netherlands.

Bruno, L., Coste, N. and Fransos, D. (2012), "Simulated flow around a rectangular 5:1 cylinder: spanwise discretisation effects and emerging flow features", *Journal of Wind Engineering and Industrial Aerodynamics*, **104–106**, 203–215.

Bruno, L., Salvetti, M.V. and Ricciardelli, F. (2014), "Benchmark on the aerodynamics of a rectangular 5:1 cylinder: and overview after the first four years of activity", *Journal of Wind Engineering and Industrial Aerodynamics*, **126**, 87–106.

Buresti G. (1981), "The effect of surface roughness on the flow regime around circular cylinders", *Journal of Wind Engineering and Industrial Aerodynamics*, **8(1-2)**, 105–114.

Buresti G., Lombardi G. and Talamelli A. (1998), "Low aspect-ratio triangular prisms in cross-flow: measurements of the wake fluctuating velocity field", *Journal of Wind Engineering and Industrial Aerodynamics*, **74-76**, 463–473.

Byrne, G., Persoons, T. and Kingston, W. (2019), "Experimental validation of lift and drag forces on an asymmetrical hydrofoil for seafloor anchoring applications", *Journal of Ocean and Climate*, **9**, 1–11.

Chiarini, A. and Quadrio, M. (2021), "The turbulent flow over the BARC rectangular cylinder: A DNS study", *Flow, Turbulence and Combustion*.

Cimarelli, A., Leonforte, A., Angeli, D. (2018), "Direct numerical simulation of the flow around a rectangular cylinder at a moderately high Reynolds number", *Journal of Wind Engineering and Industrial Aerodynamics*, **174**, 39–49.

Cimarelli, A., Leonforte, A., Angeli, D. (2018), "On the structure of the self-sustaining cycle in separating and reattaching flows", *Journal of Fluid Mechanics*, **857**, 907–936.

Dekking, M. (2018), "A modern introduction to probability and statistics: understanding why and how", *Springer*

Iungo G.V. and Buresti, G. (2009), "Experimental investigation on the aerodynamic loads and wake flow features of low aspect-ratio triangular prisms at different wind directions", *Journal of Fluids and Structures*, **25(7)**, 1119–1135.

Lamballais, E., Silvestrini, J., Laizet, S. (2010), "Direct numerical simulation of flow separation behind a rounded leading edge: study of curvature effects", *International Journal of Heat and Fluid Flow*, **31(3)**, 295–306.

Lander, D.C., Moore, D.M., Letchford, C.W. and Amitay, M. (2018), "Scaling of square-prism shear layers", *Journal of Fluid Mechanics*, **849**, 1096–1119.

Lunghi, G., Pasqualetto, E., Rocchio, B., Mariotti, A. and Salvetti, M.V. (2021), "Impact of the lateral mean recirculation characteristics on the near-wake and bulk quantities of the BARC configuration", *submitted for publication.*

Mannini, C., Soda, A. and Schewe, G. (2010), "Unsteady RANS modelling of flow past a rectangular cylinder: investigation of Reynolds number effects", *Computers and fluids*, **39(9)**, 1609–1624.

Mannini, C., Marra, A.M., Pigolotti, L. and Bartoli, G. (2017), "The effects of free-stream turbulence and angle of attack on the aerodynamics of a cylinder with rectangular 5:1 cross section", *Journal of Wind Engineering and Industrial Aerodynamics*, **161**, 42–58.

Mannini, C., Mariotti, A., Siconolfi, L. and Salvetti, M.V. (2019), " Benchmark on the aerodynamics of a 5:1 Rectangular cylinder: further experimental and LES results", *ERCOFTAC Series*, **25**, 427–432.

Mariotti, A. and Buresti, G. (2013), "Experimental investigation on the influence of boundary layer thickness on the base pressure and near-wake flow features of an axisymmetric blunt-based body", *Experiments in Fluids*, **54**, 1612.

Mariotti, A., Buresti, G. and Salvetti, M.V. (2014), "Control of the turbulent flow in a plane diffuser through optimized contoured cavities", *European Journal of Mechanics/B Fluids*, **48**, 254–265.

Mariotti, A., Buresti, G. and Salvetti, M.V. (2015), "Use of multiple local recirculations to increase the efficiency in diffusers", *European Journal of Mechanics/B Fluids*, **50**, 27–37.

Mariotti, A., Salvetti, M.V., Shoebi-Omrani, P. and Witteveen, J.A.S. (2016), " Stochastic analysis of the impact of freestream conditions on the aerodynamics of a rectangular 5:1 cylinder", *Computer and Fluids*, **136**, 170–192.

Mariotti, A., Siconolfi, L. and Salvetti, M.V. (2017), "Stochastic sensitivity analysis of large-eddy simulation predictions of the flow around a 5:1 rectangular cylinder", *European Journal of Mechanics/B Fluids*, **62**, 149–165.

Mariotti, A., Buresti, G., Gaggini, G. and Salvetti, M.V. (2017), "Separation control and drag reduction for boat-tailed axisymmetric bodies through contoured transverse grooves", *Journal of Fluid Mechanics*, **832**, 514–549.

Mariotti, A. (2018), "Axisymmetric bodies with fixed and free separation: base pressure and near-wake fluctuations", *Journal of Wind Engineering and Industrial Aerodynamics*, **176**, 21–31.

Mariotti, A., Buresti, G. and Salvetti, M.V. (2019), "Separation delay through contoured transverse grooves on a 2D boat-tailed bluff body: Effects on drag reduction and wake flow features", *European Journal of Mechanics, B/Fluids*, **74**, 351–362.

Mariotti, A., Rocchio, B., Pasqualetto, E., Mannini, C. and Salvetti, M.V. (2020), "Flow Around a 5:1 Rectangular Cylinder: Effects of the Rounding of the Upstream Corners", *ERCOFTAC Series*, **27**, 85–90.

Matsumoto, M. (1996), "Aerodynamic damping of prisms", *Journal of Wind Engineering and Industrial Aerodynamics*, **59(2-3)**, 159–175.

Matsumoto, M., Shirato, H., Aaraki, K., Haramura, T. and Hashimoto, T. (2003), "Spanwise coherence characteristic of surface pressure field on 2D bluff bodies", *Journal of Wind Engineering and Industrial Aerodynamics*, **91**, 155–163.

Moore, D.M., Letchford, C.W. and Amitay, M. (2019), "Energetic scales in a bluff body shear layer", *Journal of Fluid Mechanics*, **875**, 543–575.

Moore, D.M. and Amitay, M. (2021), "Production and migration of turbulent kinetic energy in bluff body shear layers", *International Journal of Heat and Fluid Flow*, **88**, 108716.

Nguyen, D.T., Hargreaves, D.M. and Owen, J.S. (2018), "Vortex-induced vibration of a 5:1 rectangular cylinder: A comparison of wind tunnel sectional model tests and computational simulations", *Journal of Wind Engineering and Industrial Aerodynamics*, **175**, 1–16.

Patruno, L., Ricci, M., de Miranda and S., Ubertini, F. (2019), "Numerical simulation of a 5:1 rectangular cylinder at non-null angles of attack", *Journal of Wind Engineering and Industrial Aerodynamics*, **151**, 146–157.

Pope, S.B. (2000), "Turbulent Flows", *Cambridge University Press.*

Rocchio, B. Mariotti, A. and Salvetti, M.V. (2020), "Flow around a 5:1 rectangular cylinder: Effects of upstream-edge rounding", *Journal of Wind Engineering and Industrial Aerodynamics*, **204**, 104237.

Ricci, M., Patruno, L., de Miranda, S. and Ubertini, F. (2017), "Flow field around a 5:1 rectangular cylinder using LES: Influence of inflow turbulence conditions, spanwise domain size and their interaction", *Computers and Fluids*, **149**, 181–193.

Schewe, G. (2013), "Reynolds-number-effects in flow around a rectangular cylinder with aspect ratio 1:5", *Journal of Fluids and Structures*, **39**, 15–26.

Wu, B., Li, S., Li, K. and Zhang, L. (2020), "Numerical and experimental studies on the aerodynamics of a 5:1 rectangular cylinder at angles of attack", *Journal of Wind Engineering and Industrial Aerodynamics*, **119**, 104097.

Yang, Y., Jones, D.L. and Liu, C. (2010), "Recovery of rectified signals from hot-wire/film anemometers due to flow reversal in oscillating flows", *Review of Scientific Instruments*, **81(1)**, 015104.

Zhang, Z. and Xu, F. (2020), "Spanwise length and mesh resolution effects on simulated flow around a 5:1 rectangular cylinder", *Journal of Wind Engineering and Industrial Aerodynamics*, **202**, 104186.